# Radio occultation measurements of forced atmospheric waves on Mars

D. P. Hinson and G. L. Tyler

Department of Electrical Engineering, Stanford University, Stanford, California

J. L. Hollingsworth

NASA Ames Research Center, Moffett Field, California

R. J. Wilson

Geophysical Fluid Dynamics Laboratory/NOAA, Princeton, New Jersey

**Abstract.** Mars Global Surveyor performed a series of radio occultation experiments in December 1998, resulting in 36 profiles of the neutral atmosphere in late northern spring ($L_s = 74.1°–77.3°$). The measurements are confined in latitude (64.6°–67.2°N) and local time (0321–0418), but their distribution in longitude is fairly uniform. We used least squares spectral analysis to characterize the zonal structure of the atmosphere and constructed longitude-height cross sections of both temperature and geopotential. Zonal variations of temperature exceed 12 K near the surface but are much smaller (2–3 K) at higher altitudes. Zonal variations of geopotential are ~200 m throughout the vertical range of the measurements. These patterns of temperature and geopotential appear to be stationary relative to the surface with little day-to-day variation within the 7-sol span of the measurements. We relied heavily on Mars general circulation models (GCMs) for guidance in understanding these data. Stationary planetary waves are responsible for some aspects of the temperature and geopotential fields, particularly at pressures exceeding 100–200 Pa. On the basis of strong similarities between a GCM simulation and the observations, we conclude that the disturbance takes the form of a planetary wave train excited by Alba Patera. The data also include the signature of non-Sun-synchronous thermal tides, which produce a pattern that appears to be stationary when sampled at fixed local time. Comparison between a GCM simulation and the measured geopotential field provides evidence for the presence of the resonantly enhanced, diurnal, wave-1 Kelvin mode.

## 1. Introduction

Mars Global Surveyor (MGS) entered a 45-hour elliptical orbit about Mars in September 1997 [*Albee et al.*, 1998]. Two extended periods of aerobraking maneuvers gradually guided the spacecraft into an orbit suitable for global mapping. MGS is now circling Mars at ~400-km altitude in a Sun-synchronous polar orbit with a period of ~2 hours. Systematic mapping observations began in March 1999.

The first series of radio occultation experiments with MGS yielded 88 profiles of the neutral atmosphere at latitudes 29°N–64°S in early southern summer [*Hinson et al.*, 1999]. These measurements are well suited to investigation of the lowest few scale heights of the neutral atmosphere, where their accuracy and fine vertical resolution offer new insight. Comparisons among this set of profiles revealed distinctive meridional gradients of density, pressure, and temperature associated with a low-altitude westerly jet at 15°–30°S. Although the jet is a familiar feature of atmospheric models, these occultations provided the first direct measure of its characteristics, including a gradient wind speed of ~33 m s$^{-1}$ at an altitude of 2 km.

This paper addresses a second series of occultation experiments conducted in late 1998 while aerobraking was still underway. The quality of the data considered here is exceptionally high, resulting in atmospheric profiles with uncertainties near the surface of 0.4 K and 2 Pa in temperature and pressure, respectively. The radius scale inherent in the retrieved profiles has an uncertainty no larger than ~10 m, which allows accurate registration within the geopotential field. Although the data set considered here is modest in size,

36 profiles near 66°N in late spring, the sampling in longitude is sufficient to construct cross sections of the zonal and vertical variations of both temperature and geopotential. When combined in this way, the data contain evidence for both planetary waves and non-Sun-synchronous tides. The former are stationary relative to the surface, while the latter produce a pattern that appears to be stationary when sampled at fixed local time. These types of waves arise in response to surface forcing.

These observations are limited to essentially a single latitude and local time, which hinders interpretation. We therefore rely on the Mars general circulation models (GCMs) of the NASA Ames Research Center [*Pollack et al.*, 1981, 1990, 1993; *Haberle et al.*, 1993, 1999] and the National Oceanic and Atmospheric Administration (NOAA) Geophysical Fluid Dyanmics Laboratory [*Wilson and Hamilton*, 1996] for guidance in understanding the data. We use the former for investigating stationary planetary waves and the latter for modeling thermal tides, exploiting previous experience with the respective GCMs in these areas. This combination of high-quality data and comprehensive computer models yields deeper insight into Martian atmospheric dynamics than can be achieved from either source alone.

Stationary planetary waves on Mars have been the subject of numerous theoretical studies [e.g., *Webster*, 1977; *Pollack et al.*, 1981; *Hollingsworth and Barnes*, 1996; *Barnes et al.*, 1996; *Nayvelt et al.*, 1997]. Observations are scarce, but the situation is improving with MGS. *Conrath* [1981] analyzed temperature soundings from the Mariner 9 Infrared Interferometer Spectrometer and found evidence for a planetary-scale wave near 60°N in late winter, but its identity was elusive. Possible interpretations include traveling baroclinic waves and a stationary wave-2 disturbance. *Banfield et al.* [1996] characterized Martian weather through analysis of brightness temperature measurements in the 15-$\mu$m channel of the Viking Infrared Thermal Mapper. Near $L_s = 0°$ they identified stationary structure at mid-latitudes in both hemispheres, but the validity of this result is uncertain owing to subsequent identification of a bias in the data caused by surface radiance [*Wilson and Richardson*, 2000]. Initial results from the MGS Thermal Emission Spectrometer (TES) include identification of stationary wave-1 thermal structure in the southern hemisphere during spring and summer [*Banfield et al.*, 2000; see also *Hinson et al.*, 1999]. The results reported here include a detailed characterization of planetary waves at high latitudes in northern spring, which helps to reveal the range of behavior and seasonal evolution of planetary waves on Mars.

Observations by previous spacecraft have provided a solid foundation for studies of thermal tides on Mars. This characterization includes surface pressure measurements by the two Viking landers [e.g., *Hess et al.*, 1977; *Leovy and Zurek*, 1979; *Leovy*, 1981; *Zurek and Leovy*, 1981; *Leovy et al.*, 1985; *Wilson and Hamilton*, 1996] as well as infrared measurements by the Mariner 9 and Viking orbiters [e.g., *Pirraglia and Conrath*, 1974; *Conrath*, 1976; *Martin and Kieffer*, 1979; *Wilson and Richardson*, 2000]. Tides are now known to be a distinctive component of Martian meteorology, and MGS will contribute to significant advances in this area. Observations by TES during aerobraking achieved sufficient coverage in latitude, longitude, and local time to allow unique identification of several tidal modes [*Banfield et al.*, 2000]. Although tides are much more difficult to decipher from the vantage point of the low-altitude, polar, Sun-synchronous, mapping orbit, global measurements by MGS at fixed local time will complement Viking lander measurements at fixed location.

## 2. Observations

Following a 6-month interval in which MGS was visible from Earth throughout its orbit, occultation experiments resumed on November 19, 1998. Measurements continued for more than 200 orbits until January 1, 1999, when spacecraft power constraints halted all occultation experiments for $\sim$1 month. From November 19 through December 31, data collection was continuous at ingress but was interrupted twice at egress by spacecraft maneuvers required first for temperature control (November 26 to December 3) and later for aerobraking (December 24–31).

Operational constraints limited the quality of all data acquired prior to December 24 in two ways. First, the carrier signal transmitted by the spacecraft and used for sounding Mars's atmosphere was reduced in strength by $\sim$15 dB owing to the effects of telemetry modulation. Second, the experiment duration was shorter than usual, so that the high-altitude baseline normally used for data calibration and error analysis was often absent. These lower-quality data require a specialized retrieval algorithm and will be the subject of future work.

This paper reports results derived from high-quality data collected at occultation entry on December 24–31, 1998. Telemetry modulation was turned off during each experiment, resulting in a signal-to-noise ratio of 50–55 dB in a 1-Hz bandwidth. A high-altitude baseline was included at the beginning of each experiment.

Figure 1 shows the spatial distribution of the measurements. The spacecraft orbit period decreased from 3.9 hours at the start of this interval to 3.6 hours at the end, so that the separation in longitude between consecutive measurements was $\sim$55°. Note that the measurements sometimes returned to nearly the same longitude after an integer number of planet rotations. The season was late spring in the northern hemisphere ($74.1° < L_s < 77.3°$). The local true solar time ranged from 0321 to 0418, corresponding to early morning at this latitude and season, with the Sun $\sim$10° above the horizon.

The overall geometry of these experiments was favorable. Earth was about to cross the MGS orbit plane, so that the occultations were nearly diametric. As the
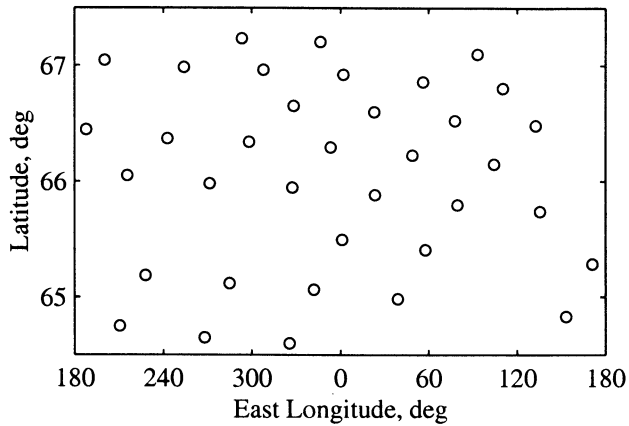
**Figure 1.** Locations of MGS radio occultation measurements on December 24–31, 1998. The first experiment was at 64.6°N, 325.4°E. Subsequent measurements moved steadily westward and northward, ending at 67.2°N, 293.3°E.

angle between Mars and the Sun as viewed from Earth was ~80°, solar interference was negligible. The distance from Earth to Mars was 1.5 AU.

## 3. Method of Data Analysis

MGS occultation experiments sound the atmosphere of Mars using a coherent radio signal transmitted by the spacecraft at a frequency of 8423 MHz [*Tyler et al.*, 1992]. This signal is derived from an "ultrastable" oscillator (USO) with a fractional frequency stability of $\sim 10^{-13}$ over timescales of 1–1000 s. The occultation data are recorded using one of the 34-m or 70-m antennas of NASA's Deep Space Network (DSN).

We used an established procedure for retrieving atmospheric profiles [*Hinson et al.*, 1999]. The method is based on geometrical optics [e.g., *Fjeldbo and Eshleman*, 1968; *Fjeldbo et al.*, 1971], in which the radio signal is visualized as following a distinct geometrical "ray path" from spacecraft to Earth. The ray path curves gradually within Mars's atmosphere in response to the local gradient of refractive index, causing a deflection between the incoming and outgoing rays and a Doppler shift in the frequency of the signal received on Earth.

Figure 2 shows an example of partially processed data. All Doppler shifts have been removed except those caused by the atmosphere and ionosphere of Mars. The sample spacing is 0.41 s in time and 670 m in altitude. The fluctuations at altitudes above ~300 km correspond to thermal noise with a standard deviation of 4.3 mHz. The effect of the ionosphere appears at altitudes of 70–200 km, with a maximum Doppler shift of +60 mHz at 150 km. The neutral atmosphere dominates at altitudes below ~60 km, producing a negative Doppler shift whose magnitude increases steadily with decreasing altitude. The peak effect of the neutral atmosphere, about −13 Hz, exceeds the noise level by a factor of ~3000.

Analysis of frequency residuals such as those in Figure 2 yields a profile of refractive index $\mu$ versus planetocentric radius $r$ that extends from the surface to well above the ionosphere. Within the neutral atmosphere, number density $n$ is proportional to $\mu - 1$. The constant of proportionality depends on the composition of the atmosphere and the microwave properties of the constituents, which are known. Pressure $p$ and temperature $T$ are derived from $n(r)$ by assuming hydrostatic balance, integrating vertically, and using the ideal gas law. For example,

$$T(r) = \frac{n_b T_b}{n(r)} + \frac{\overline{m}}{n(r)\,k} \int_r^{r_b} n(r')\,g(r')\,dr' , \quad (1)$$

where $\overline{m}$ is the average molecular mass of the gas mixture, $k$ is the Boltzmann constant, and $g$ is the acceleration of gravity. The temperature profile extends to a maximum radius $r_b$, above which errors caused by thermal noise would become excessive. At this radius the
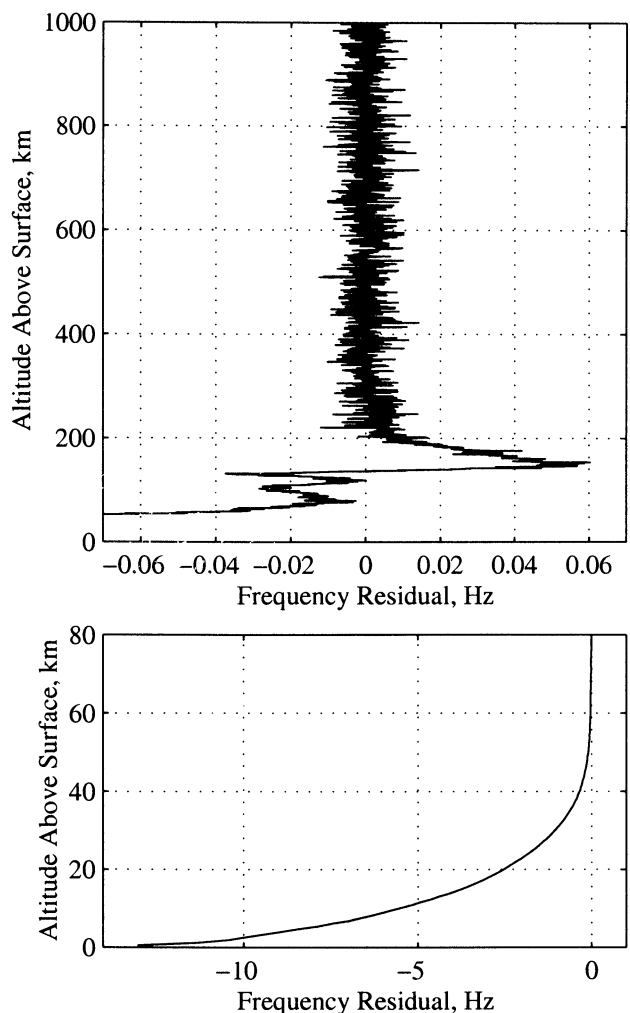


**Figure 2.** Frequency measurements on December 25, 1998, by a 34-m DSN antenna near Madrid, Spain. The same data appear in both panels, but with different horizontal and vertical scales. The measurement location was 65.1°N, 341.9°E. The solar zenith angle was 79°.

density $n_b$ is already known, but the temperature $T_b$ is required as a boundary condition. Note that the influence of the boundary condition diminishes rapidly with increasing pressure.

This procedure yields vertical profiles of $n$, $p$, and $T$. Each sample in the profile is assigned to the location within the atmosphere where the corresponding ray path was perpendicular to the local vertical direction. The locations are expressed in planetocentric coordinates in the International Astronomical Union (IAU) 1991 reference frame [*Davies et al.*, 1992]. We computed the geopotential $\Phi$ at the location of each sample using a fiftieth degree and order representation of the gravity field [*Smith et al.*, 1993]. We normalized $\Phi$ so that its zonally averaged value at an equatorial radius of 3396.0 km is 0 m$^2$ s$^{-2}$. The same gravity field model was used to compute $g$ during integration of (1).

The vertical resolution of these profiles is diffraction limited to $\sim$1 km, as determined by the experiment geometry and the wavelength of radiation [e.g., *Karayel and Hinson*, 1997; *Hinson et al.*, 1999]. The sample spacing in the retrieved profiles is $\sim$700 m, roughly consistent with the inherent resolution.

The horizontal resolution of limb-sounding measurements on Mars is a few hundred kilometers [e.g., *Hinson et al.*, 1999]. This corresponds to several degrees of latitude for the geometry of these experiments, where the propagation path from MGS to Earth passed through the atmosphere of Mars at an angle $\sim$17° east of local north.

## 4. Results

This series of experiments yielded 36 profiles, which can be obtained from the Planetary Data System (PDS) (http://pds.jpl.nasa.gov) or through the MGS radio science Web site (http://nova.stanford.edu/projects/mgs-/dmwr.html).

### 4.1. Atmospheric Profiles

Figure 3 shows three temperature profiles, each retrieved from the frequency residuals in Figure 2. Owing to the high quality of data from this experiment, the profiles extend upward to a pressure of 3 Pa, corresponding to an altitude of 50 km above the surface. The curves show the result of changes in $T_b$ over the range of plausible values. The temperature lapse rate at low pressures becomes superadiabatic when $T_b < 115$ K, providing a lower bound. Conversely, a temperature inversion appears at low pressures when $T_b = 165$ K, but it is far stronger than any inversion that appears in the GCM simulations discussed later in this paper. Zonal mean temperatures are expected to decrease monotonically with height over this altitude range at 66°N in late spring [e.g., *Haberle et al.*, 1993; *Hourdin et al.*, 1993; *Forget et al.*, 1999]. From these considerations we estimate that $T \approx 140 \pm 25$ K at 3 Pa and $T \approx 142 \pm 10$ K at 8 Pa.
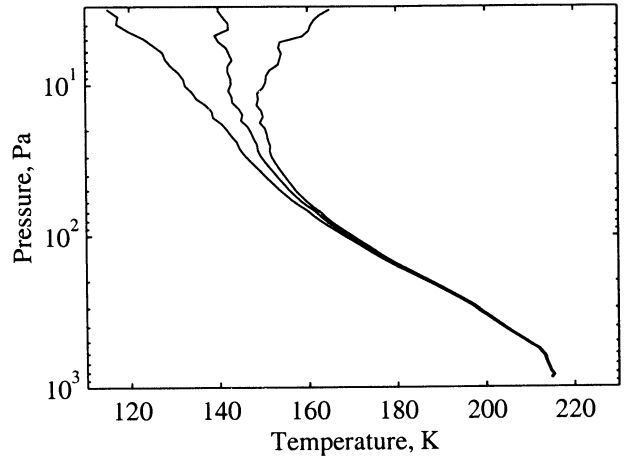


**Figure 3.** Temperature profiles retrieved from the frequency residuals in Figure 2. Results are shown for three values of $T_b$: 115, 140, and 165 K. The measurement location was 65.1°N, 341.9°E at $L_s = 74.6°$ and local time 0410.

Data from some experiments are of lower quality than those shown in Figure 2, so that profiles could not always be obtained at pressures as low as 3 Pa. The profiles sent to PDS extend from the surface to the 8-Pa pressure level, with $T_b$ set to 142 K. At the top of the profiles the standard deviations in $T$ and $p$ are $\sim$7% (10 K and 0.6 Pa, respectively), corresponding to our estimate of the uncertainty in $T_b$. Near the surface, where the profiles are most accurate, the standard deviations in $T$ and $p$ are typically $\sim$0.2% (0.4 K and 2 Pa, respectively). All results in the remainder of this paper are based exclusively on the profiles sent to PDS.

Figure 4 shows samples of the vertical structure at selected longitudes. In each of the first three panels, a comparison is made between a pair of profiles from nearly the same location on Mars, with intervals between the measurements of 4, 2, and 3 Martian days (sols), respectively. In all three cases the measurements are highly repeatable. These comparisons demonstrate both the accuracy of the measurements and the absence of significant day-to-day variation in the thermal structure at these longitudes. (The profiles provide essentially no information about diurnal variations, since all measurements were made at nearly the same local time, $\sim$0400.)

Figure 4 also shows that the vertical structure varies significantly with longitude, especially within the lowest scale height above the surface. In Figures 4a–4c each pair of profiles differs noticeably from those in the other panels. The temperature near the surface varies with longitude by more than 10 K, as illustrated in Figure 4d. These zonal variations include large changes in static stability near the surface.

### 4.2. Zonal Structure: Temperature

We now take a closer look at the zonal structure. Figure 5 shows measurements of temperature versus lon-
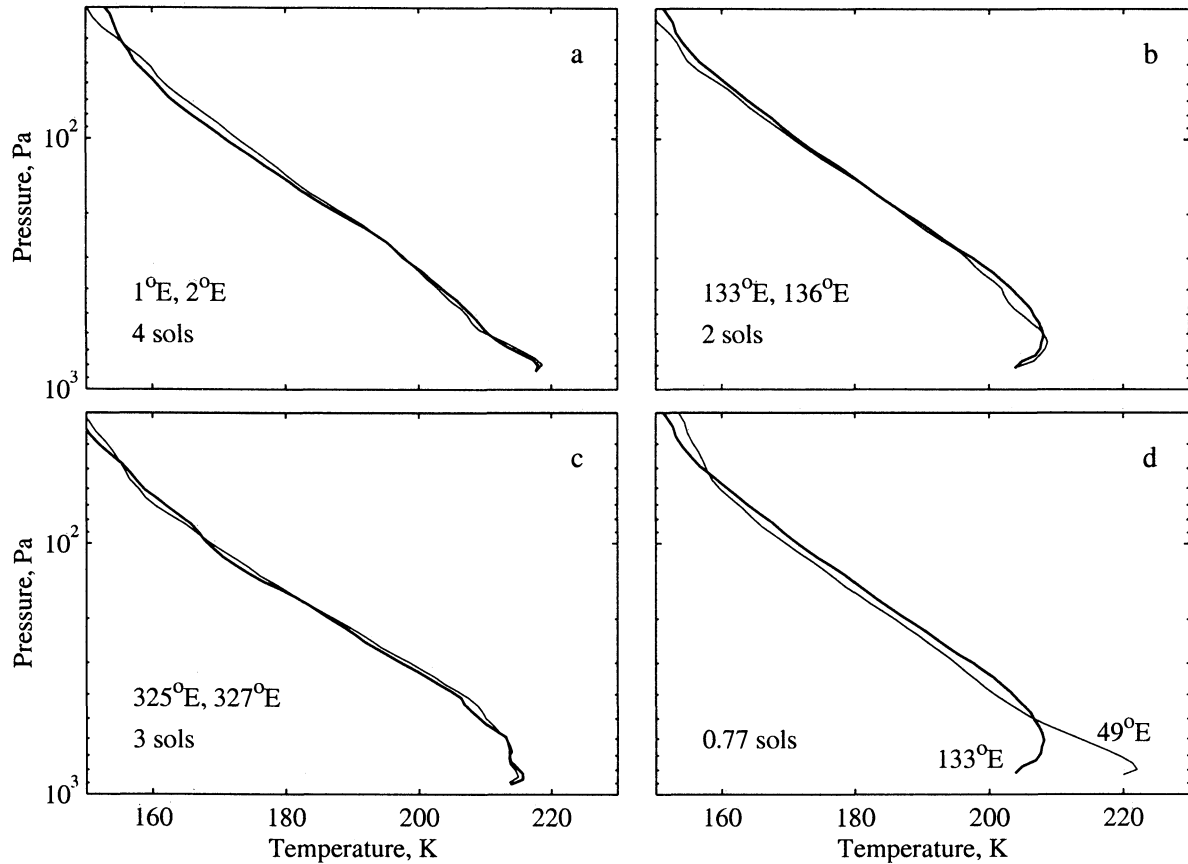
**Figure 4.** (a–c) Pairs of profiles obtained at nearly the same location on Mars. The interval between each pair of measurements was an integer number of Martian days (sols), as indicated. (d) Profiles at different longitudes from measurements separated by 0.77 sols. All profiles extend to the surface, where the differences in pressure are due primarily to topography. The measurement locations and local times were (a) 65.5°N, 1.1°E, 0402 and 66.9°N, 2.0°E, 0330, (b) 66.5°N, 132.8°E, 0341 and 65.7°N, 135.6°E, 0357, (c) 64.6°N, 325.4°E, 0418 and 65.9°N, 327.4°E, 0353, and (d) 66.2°N, 48.9°E, 0347 and 66.5°N, 132.8°E, 0341.

gitude on three surfaces of constant pressure. (For reference, the surface pressure ranged from 810 to 940 Pa with an average value of 880 Pa for these 36 profiles.) While there are significant zonal variations at all pressures, measurements at the same longitude are highly repeatable, as in Figure 4. Hence the zonal structure appears to be stationary relative to the surface with little day-to-day variation.

The most striking feature of the data in Figure 5 is the large, regular oscillation of temperature with longitude at 0°–180°E on the 700-Pa pressure level. A sinusoid with a zonal period of 180° (wave number 2) and an amplitude of 6 K fits the data well, as shown by the dashed line in Figure 5c.

At each pressure level we separated the temperature into zonal-mean and zonally varying components:

$$T(\lambda, p) = \overline{T}(p) + T'(\lambda, p) , \qquad (2)$$

where $\lambda$ is east longitude. We modeled the zonal variations as

$$T'(\lambda, p) = \sum_{s=1}^{4} C_s(p) \cos[s\lambda - \gamma_s(p)] . \qquad (3)$$

Here, $C_s$ and $\gamma_s$ are the amplitude and phase, respectively, at zonal wave number $s$, where $s$ is a dimensionless integer. The quantities $\overline{T}$, $C_s$, and $\gamma_s$ vary with $p$. We retained terms through $s = 4$. The results do not change appreciably when higher-order terms are included.

The distribution of these data in longitude is irregular. When sampled in this way, the sine and cosine functions are no longer orthogonal vectors, and Fourier analysis is not reliable. We therefore fitted the model to the data by least squares, solving simultaneously for nine free parameters at each pressure level. This is a simple extension of the procedure used in constructing the Lomb-Scargle periodogram [e.g., Lomb, 1976; Press and Teukolsky, 1988; Wu et al., 1995]. The smooth lines in Figures 5a and 5b show the results of fitting this model to the data. The average temperature is
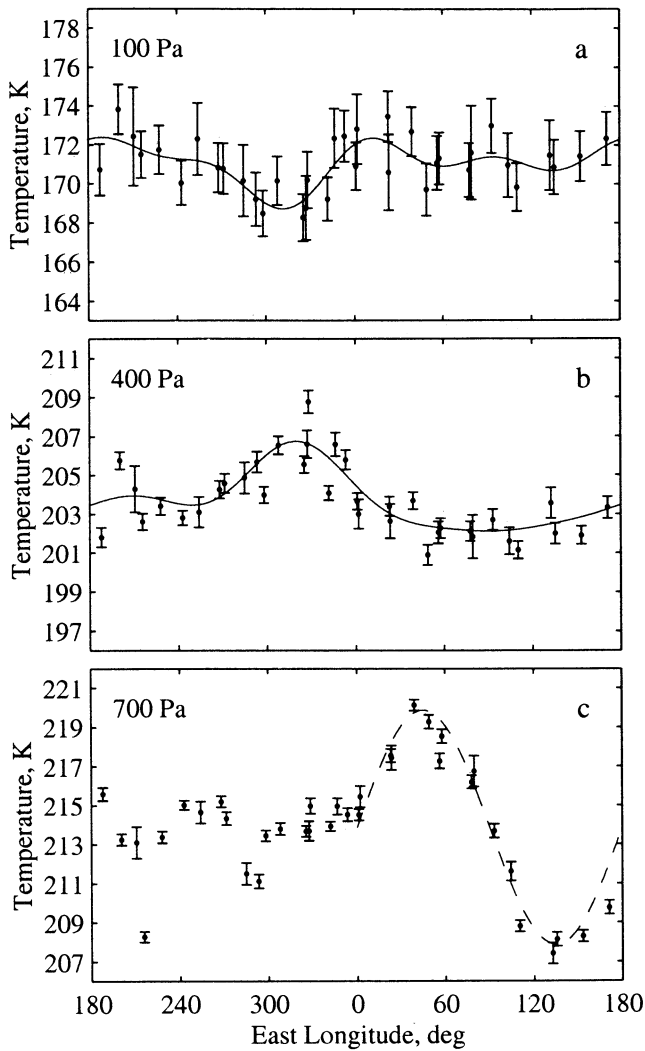
**Figure 5.** Temperature versus longitude at a constant pressure of (a) 100 Pa, (b) 400 Pa, and (c) 700 Pa. One sample of temperature was obtained from each occultation profile through interpolation. The average uncertainty in temperature is 1.5, 0.6, and 0.4 K (one sigma) at 100, 400, and 700 Pa, respectively.

171.1 K at 100 Pa, where the amplitudes at $s = 1$–4 are 0.6, 1.0, 0.4, and 0.6 K, respectively. At 400 Pa, $\overline{T}$ increases to 203.7 K, and the amplitudes at $s = 1$–4 are 1.6, 0.9, 0.6, and 0.2 K, respectively.

We extended this analysis to include 42 pressure levels with an average vertical spacing of ~800 m. At each pressure we obtained a sample of temperature from each of the 36 profiles through interpolation, and we modeled the variation of temperature with longitude through least squares spectral analysis. Figure 6 shows the resulting composite model for the temperature field.

We note two important features of the temperature field in Figure 6. First, the zonal variations are largest, ~12 K peak to peak, at pressures exceeding 500 Pa and longitudes 0°–180°E (see Figures 4d and 5c). These large temperature variations in the lowest half scale height overlie relatively flat topography; the highest

and lowest surface elevations at this latitude differ by ~1.6 km overall and by ~0.9 km at 0°–180°E. [*Smith et al.*, 1999]. Second, temperature varies significantly with longitude at all pressures. Near the surface the strongest components are at $s = 1$ and 2, each with an amplitude of 3–4 K. At pressures <350 Pa the strongest component is at $s = 2$, with an amplitude of 1–1.5 K.

### 4.3. Zonal Structure: Geopotential

The occultation profiles provide complementary information in the form of geopotential versus pressure. It is convenient to define the geopotential height $Z$ as [e.g., *Holton*, 1992]

$$Z \equiv \Phi/g_0 , \qquad (4)$$

where $g_0$ is 3.7155 m s$^{-2}$, the global average of gravity at $\Phi = 0$.

As with temperature, we separated the geopotential height into zonal-mean and zonally varying components,
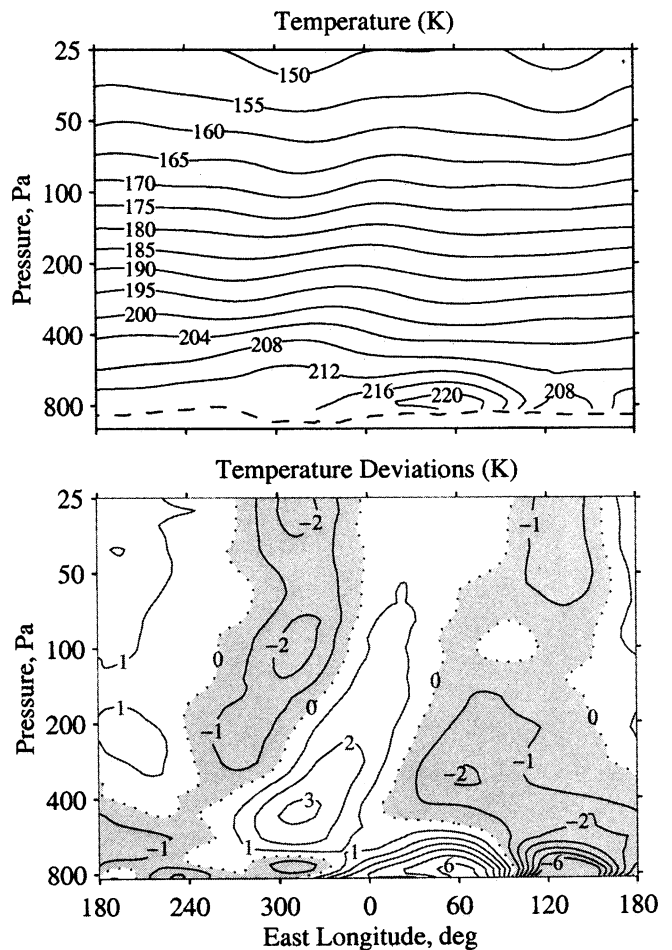


**Figure 6.** (top) Measured thermal structure at 66°N, $L_s = 75°$. The contour interval is 5 K for $T < 200$ K and 4 K for $T > 200$ K. The dashed line shows the pressure at the surface. (bottom) Temperature deviations from the zonal average. The contour interval is 1 K. Shading denotes negative values.
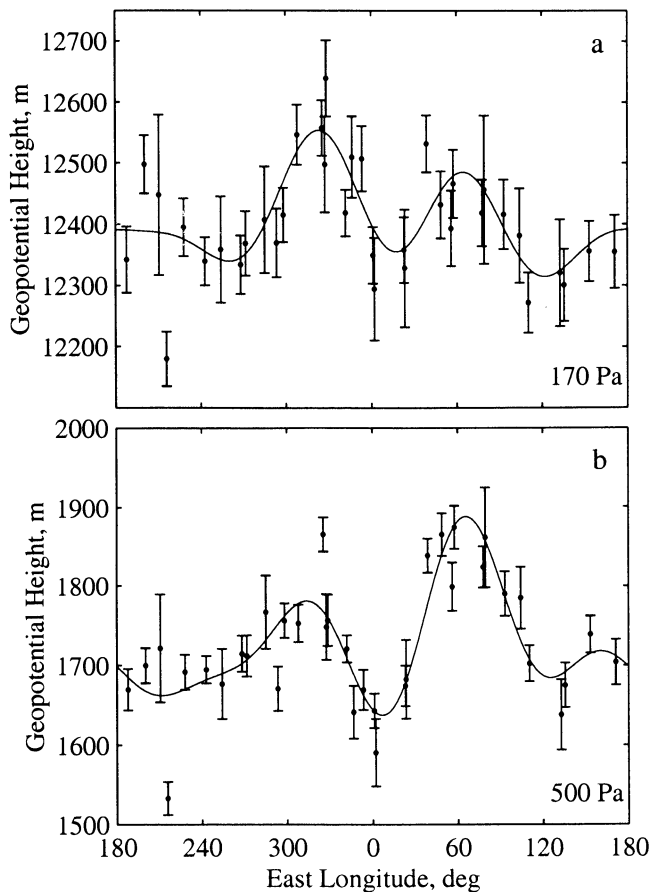
**Figure 7.** Geopotential height versus longitude at a constant pressure of (a) 170 Pa and (b) 500 Pa. One sample was obtained from each occultation profile through interpolation. The average uncertainty is 63 m (one sigma) at 170 Pa and 31 m at 500 Pa.

$$Z(\lambda, p) = \overline{Z}(p) + Z'(\lambda, p) , \qquad (5)$$

and we modeled the zonal variations at constant pressure as

$$Z'(\lambda, p) = \sum_{s=1}^{4} D_s(p) \cos[s\lambda - \delta_s(p)] . \qquad (6)$$

Here, $D_s$ and $\delta_s$ are the amplitude and phase, respectively, of the component at wave number $s$. As before, we solved for these parameters through least squares spectral analysis and retained terms through $s = 4$.

Figure 7 shows the variation of $Z$ with longitude on two surfaces of constant pressure. The least squares fit is shown by a smooth line in each panel. Samples with a small separation in longitude are generally consistent, but $Z$ varies significantly with longitude in both cases. For example, the main features of the data in Figure 7b are a deep geopotential "trough" centered near 7°E ($Z = 1640$ m) and two significant "ridges" centered near 66°E ($Z = 1890$ m) and 314°E ($Z = 1780$ m). The 250-m difference between the smallest and largest values of $Z$ produces a steep gradient near 36°E.

Figure 8 shows a contour plot of $Z'$ analogous to Figure 6. The amplitude of each zonal harmonic, $D_s$, is plotted versus pressure in Figure 9. At pressures between 70 and 700 Pa the strongest component is at $s = 3$, with an amplitude of 50–60 m. The amplitude of the wave-2 component grows exponentially with height at low pressures, increasing from a minimum of ∼14 m at 200 Pa to more than 100 m at 25 Pa.

## 5. Previous Measurements

In this section we compare the MGS occultation results with relevant measurements by the Mariner 9 and Viking orbiters. (TES will collect highly complementary measurements throughout the MGS mapping phase, but it was turned off near $L_s = 75°$.) Our immediate goal is to check for consistency among the various data sets. At the same time, we use these measurements along with a GCM simulation to estimate the zonal wind field at this season. This provides a context for interpreting the results in Figures 6 and 8.

The meridional structure of the atmosphere at $L_s = 43°–54°$ was characterized previously through a series of measurements by the Infrared Interferometer Spectrometer (IRIS) on Mariner 9 [*Leovy*, 1979; *Pollack et al.*, 1981]. A horizontal temperature gradient was observed at middle to high latitudes in the northern hemisphere, with temperatures decreasing toward the pole throughout the vertical range of the measurements (surface to ∼30 Pa). If the wind speed at the surface is assumed to be negligible, then zonal winds in geostrophic balance with the temperature field are westerly at latitudes poleward of ∼45°N throughout this vertical range [*Leovy*, 1979; *Pollack et al.*, 1981].

The difference between these IRIS measurements and the thermal structure in Figure 6 is remarkably small.
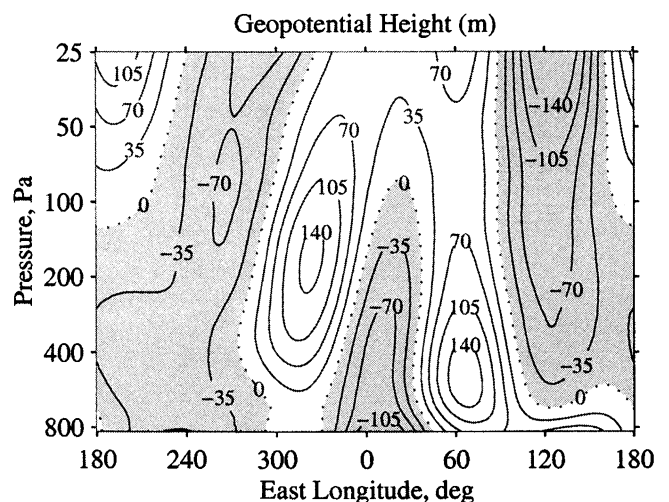


**Figure 8.** Measured geopotential field at 66°N, $L_s = 75°$. The contour interval is 35 m. Shading denotes negative values.
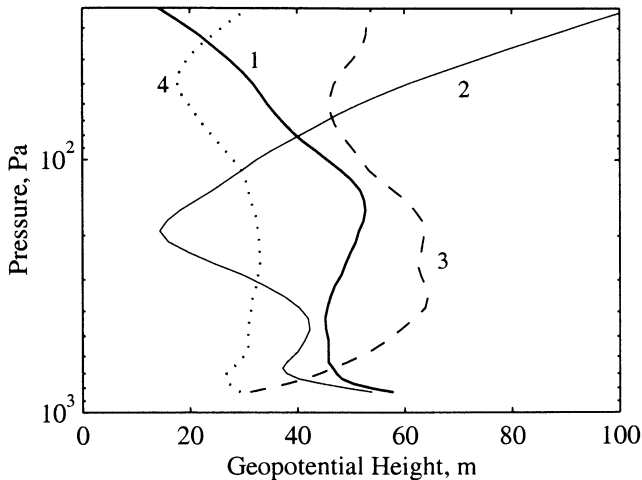
**Figure 9.** Variation of geopotential height with pressure for each zonal harmonic, corresponding to the measurements in Figure 8. The number adjacent to each curve indicates the value of the zonal wave number $s$.

The temperatures at 66°N agree to within a few kelvins at all altitudes despite the difference in season and the elapsed time of ~14 Martian years between the two sets of experiments. This similarity suggests that temperatures vary slowly with season near aphelion ($L_s \approx 70°$) and that westerly winds persist at high northern latitudes at $L_s = 75°$.

These conclusions are reinforced by measurements in the 15-$\mu$m channel of the Viking Infrared Thermal Mapper (IRTM), which has a weighting function that peaks at ~50 Pa with a full width at half maximum of ~25 km. *Wilson and Richardson* [2000] recalibrated the 15-$\mu$m brightness temperatures (IRTM $T_{15}$) to remove a bias caused by surface radiance. The revised results include a map of diurnally averaged temperature versus latitude and season [*Wilson and Richardson*, 2000, Figure 21]. At $L_s = 75°$, there is a slight decrease in temperature with increasing latitude poleward of ~45°N, similar to the IRIS measurements near $L_s = 50°$. The revised IRTM $T_{15}$ at 66°N, ~160 K, agrees closely with the occultation measurements at 50 Pa, where the average temperature is 158 K and the average uncertainty is 2.4 K. (The uncorrected IRTM $T_{15}$ exceeds the occultation result by ~15 K.) Moveover, the thermal structure in Figure 21 of Wilson and Richardson changes very gradually with season for $L_s = 50°-75°$. In summary, these IRIS, revised IRTM $T_{15}$, and MGS measurements are mutually consistent [see also *Richardson*, 1998].

Using these data as constraints, we also characterized the zonal-mean circulation at $L_s = 75°$ with the GCM of the NASA Ames Research Center [e.g., *Haberle et al.*, 1999]. The version used here has 26 vertical layers extending from the surface to 0.005 Pa and a horizontal resolution of 7.5° in latitude by 9° in longitude. The model uses the topography measured by the MGS laser altimeter [*Smith et al.*, 1999] and incorporates maps

of surface albedo and thermal inertia from the Mars Consortium data set [e.g., *Pollack et al.*, 1990].

The thermal structure and circulation depend sensitively on the distribution of dust within the atmosphere. For our simulations concerning planetary waves (Figures 10 and 14, Plates 1 and 2), the dust distribution is prescribed to be uniform over the southern hemisphere with a visible opacity $\tau$ of 0.3. In the northern hemisphere, $\tau$ decreases linearly with latitude from 0.3 at the equator to zero at the north pole. Several factors motivated this choice. First, this dust distribution produces a temperature field that compares favorably with the measurements described above, whereas a globally uniform distribution with $\tau = 0.3$ yields temperatures that exceed the observations by 10–20 K near 66°N. The poleward decrease of $\tau$ in the northern hemisphere is intended to mimic the preferential concentration of dust in the tropics by the Hadley circulation. In addition, our opacity model for the northern hemisphere is qualitatively consistent with the dust distribution retrieved from IRIS data by *Santee and Crisp* [1993, 1995] for $L_s = 343°-348°$, which has peak opacity near the equator and a poleward decrease in both hemispheres.

Figure 10 shows the mean thermal structure and zonal winds obtained from a 30-sol GCM simulation centered on $L_s = 75°$. Winds are easterly between about 50°N and 20°S and westerly elsewhere, with much stronger westerlies in the south than in the north. The strong westerly winds at middle to high latitudes in the south are accompanied by prominent stationary planetary waves (not shown), as expected from previous winter-solstice simulations [*Hollingsworth and Barnes*, 1996; *Barnes et al.*, 1996]. Westerly winds predominate at 66°N, with easterlies appearing only within a very shallow layer adjacent to the surface and at pressures <0.4 Pa. The simulation also produces stationary planetary waves within these weaker westerlies, as discussed in section 6, but their behavior is much different than in the south.

## 6. Stationary Planetary Waves

Planetary, or Rossby, waves are characterized by large spatial scales, low frequencies, and meridional motion that is strongly influenced by the northward gradient of potential vorticity [e.g., *Andrews et al.*, 1987]. Zonal variations of surface elevation, thermal inertia, and albedo can excite stationary waves, which are a candidate for explaining the observations in Figures 6 and 8. The behavior of stationary planetary waves depends critically on the speed and direction of the basic zonal winds, with vertical propagation occurring only in westerly flows.

As discussed in section 5, the zonal winds were probably westerly at the season and location of the occultation measurements. Within this context, we now use linear theory together with a GCM simulation to show that key features of the data are consistent with a planetary-wave interpretation.
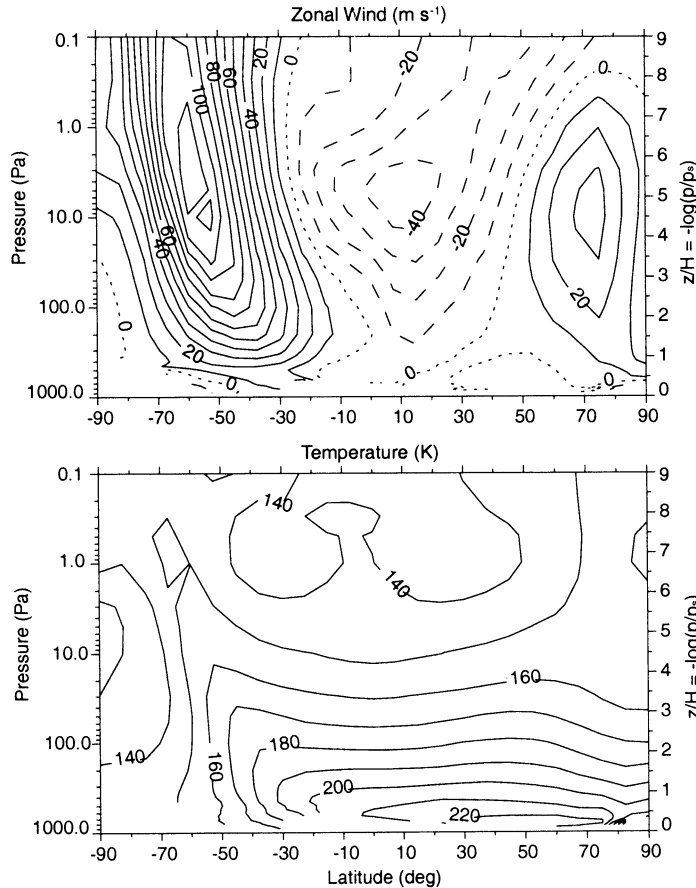
**Figure 10.** (top) Zonal wind and (bottom) temperature as simulated by the NASA Ames GCM. Both fields have been averaged over time and longitude. The contour intervals are 10 m s$^{-1}$ and 10 K. Westerly and easterly winds are denoted by solid and dashed contours, respectively. The accuracy of both the temperature and zonal wind fields is limited by uncertainty in the spatial distribution of dust.

### 6.1. Linear Theory

Linear, quasi-geostrophic theory offers insight into the behavior of forced planetary waves in a basic zonal flow [e.g., *Andrews et al.*, 1987]. Wave perturbations to geopotential height and temperature vary spatially as

$$Z', \, T' \propto \exp\left[\frac{z}{2H} + i(kx + ly + mz)\right], \qquad (7)$$

where $z$ is a log-pressure vertical coordinate, $H$ is the pressure scale height, $x$ and $y$ are eastward and northward distance, respectively, and $k$, $l$, and $m$ are the zonal, meridional, and vertical wave numbers, respectively. The approximate dispersion relation for stationary waves can be expressed as [*Andrews et al.*, 1987, p. 185]

$$m^2 = \frac{N^2}{f^2}\left[\frac{\overline{q}_y}{\overline{u}} - \left(\frac{s}{r_m \cos\phi}\right)^2 - l^2 - \frac{f^2}{4N^2 H^2}\right], \qquad (8)$$

where $N$ is the buoyancy frequency, $f$ is the Coriolis parameter, $\overline{q}_y$ is the northward gradient of mean quasi-geostrophic potential vorticity, $\overline{u}$ is the mean zonal wind, $r_m$ is the radius of Mars, $\phi$ is latitude, and the dimensionless zonal wave number $s = k\,r_m \cos\phi$. At

66°N, $f \approx 1.3 \times 10^{-4}$ s$^{-1}$ and $r_m \approx 3377$ km. For these profiles, $N \approx 7 \times 10^{-3}$ s$^{-1}$ and $H \approx 10$ km. From the GCM simulation in Figure 10, $\overline{q}_y \approx 3 \times 10^{-11}$ m$^{-1}$ s$^{-1}$ near the 400-Pa pressure level at 66°N.

Vertical propagation requires that $m^2 > 0$. From (8) this leads to the "Charney-Drazin" condition:

$$0 < \overline{u} < \frac{30 \text{ m s}^{-1}}{s^2 + 1}. \qquad (9)$$

In evaluating this expression, we used the parameter values given above and chose $l = k$. For $s = 1$, vertical propagation can occur at 66°N in westerlies weaker than $\sim$15 m s$^{-1}$, corresponding to pressures of 100–700 Pa in Figure 10. For $s = 2$, vertical propagation can occur in westerlies weaker than $\sim$6 m s$^{-1}$, which is satisfied at pressures of 300–700 Pa in Figure 10. In both cases the waves become evanescent at higher altitudes and within the shallow layer of easterlies adjacent to the surface.

The measurements in section 4 provide no constraint on the meridional structure, so that $l$ is unknown. However, these conclusions about vertical propagation do not change significantly when $l = \pi/(2400$ km$)$, a value inferred from the GCM simulation discussed in section 6.2 (see Plate 1).

Geopotential Height (m), s=1
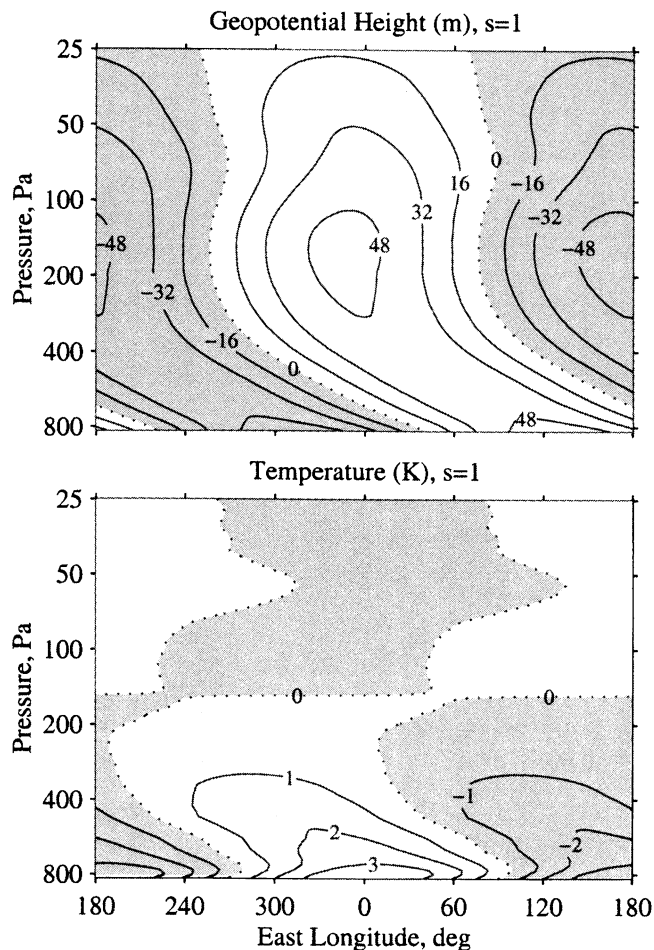


Temperature (K), s=1



**Figure 11.** Wave-1 components of the measurements in Figures 6 and 8. The contour intervals are 16 m and 1 K. Shading denotes negative values.

When comparing the data with linear theory, it is convenient to separate the fields in Figures 6 and 8 into zonal harmonics. Figure 11 shows the structure of $Z'$ and $T'$ at $s = 1$. At pressures greater than $\sim300$ Pa, contours of $Z'$ and $T'$ tilt westward with height, resembling an upward propagating, stationary, planetary wave [e.g., Andrews et al., 1987, p. 179]. (Here upward refers to the vertical component of the group velocity.) Adopting the convention that $k > 0$, the westward tilt implies that $m > 0$.

At pressures greater than $\sim300$ Pa in Figure 11, the warmest temperatures lie about one quarter cycle westward of the peak in geopotential, or $\delta_1 - \gamma_1 \approx \pi/2$ in the notation of (3) and (6). This can be understood through use of the linearized hydrostatic equation

$$\frac{RT'}{H} = g_\circ \frac{\partial Z'}{\partial z} = g_\circ \left(\frac{1}{2H} + im\right) Z' . \quad (10)$$

Here $R$ is the gas constant (191 J kg$^{-1}$ K$^{-1}$). For the data in Figure 11, $2Hm \gg 1$ at pressures exceeding $\sim300$ Pa. Equation (10) then gives a phase shift of $\pi/2$ between $T'$ and $Z'$ (at constant pressure).

The vertical structure in Figure 11 is also qualitatively consistent with predictions of linear theory. The wave propagates vertically below the 300-Pa pressure level, where contours of constant $Z'$ have a distinct westward tilt, but appears to be evanescent at higher altitudes. The node of $T'$ at the 150-Pa pressure level may mark the transition between regions of vertical propagation and evanescence.

Figure 12 shows the variations of $Z'$ and $T'$ at $s = 2$. The structure is more complicated than at $s = 1$. At the 700-Pa pressure level the contours of constant $Z'$ tilt westward with height and $\delta_2 - \gamma_2 \approx \pi/2$. This suggests that a stationary planetary wave may be present, but its structure is more narrowly confined near the surface than at $s = 1$. For example, the node in temperature has descended from $\sim150$ Pa at $s = 1$ to $\sim600$ Pa at $s = 2$. In addition, the geopotential field at $s = 2$ between the surface and the 200-Pa pressure level resembles a vertically compressed version of the full field at $s = 1$. This behavior is consistent with (8) and (9), where an increase in $s$ reduces the vertical extent of the response to surface forcing. At low pressures the geopo-
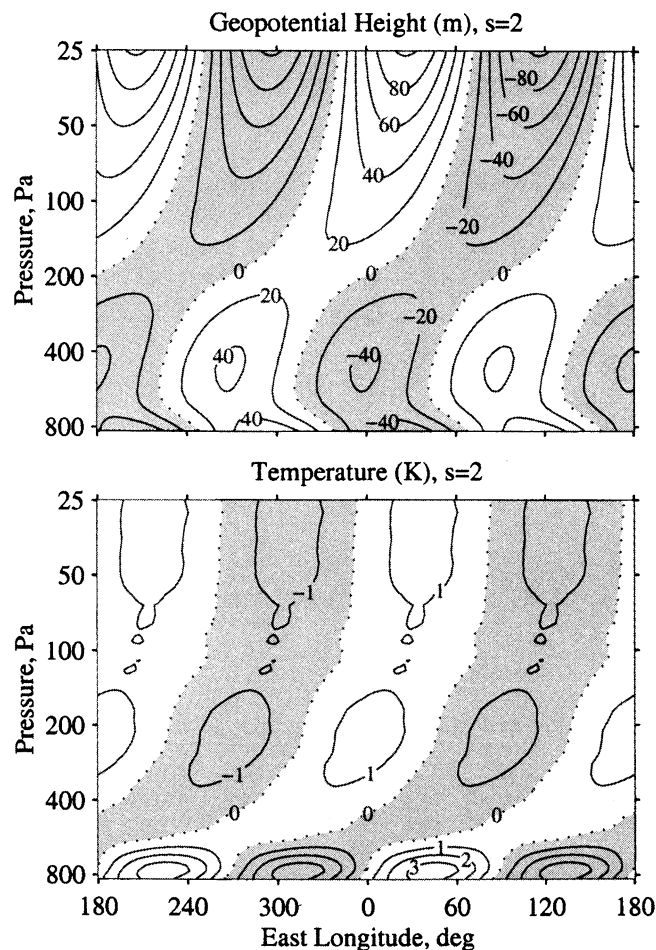
Geopotential Height (m), s=2



Temperature (K), s=2



**Figure 12.** Wave-2 components of the measurements in Figures 6 and 8. The contour intervals are 20 m and 1 K. Shading denotes negative values.
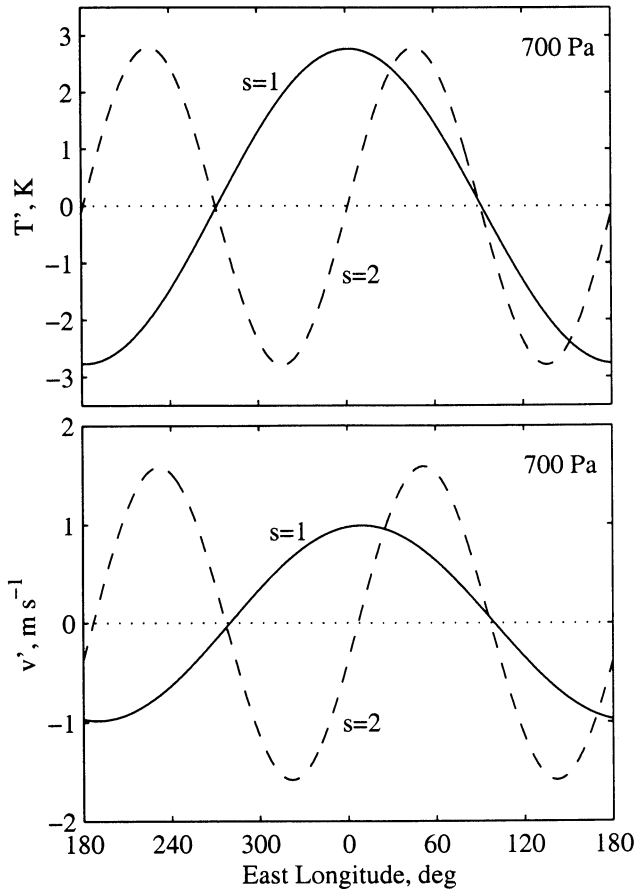
**Figure 13.** Zonal variations of (top) temperature and (bottom) meridional wind speed at the 700-Pa pressure level. The temperature harmonics were obtained through spectral analysis of occultation data (see Figures 11 and 12). Meridional winds (positive northward) were derived from the corresponding geopotential measurements by assuming geostrophic balance.

tential and temperature fields at $s = 2$ probably include contributions from thermal tides. We will return to this point in section 7.

We can estimate the meridional wind speed $v'$ from the geopotential field by assuming geostrophic balance [e.g., *Holton*, 1992]:

$$v' = \frac{1}{f} \left( \frac{\partial \Phi}{\partial x} \right)_p . \tag{11}$$

We applied (11) to the geopotential fields in Figures 11 ($s = 1$) and 12 ($s = 2$). Figure 13 shows results at the 700-Pa pressure level, where $v'$ and $T'$ are nearly in phase at both zonal wave numbers. Hence the configuration of the near-surface temperature and geopotential fields implies poleward advection of warm air and equatorward advection of cool air, with wind speeds of 1–2 m s$^{-1}$.

In summary, linear theory suggests that planetary waves may account for a significant part of the structure in Figures 11–13. Near the surface the amplitude

is 50–60 m and 3–4 K for both modes, and the temperature variations at $s = 1$ and 2 interfere constructively (destructively) in the eastern (western) hemisphere.

## 6.2. GCM Simulation

In section 6.1 we used linear theory for an initial assessment of the data. We now turn to GCM simulations to gain deeper insight. Comprehensive, fully nonlinear computer models avoid the questionable approximations of linear theory, leading to more convincing conclusions.

The GCM results concerning planetary waves are based on a 30-sol simulation centered on $L_s = 75°$, as described in section 5. The mean thermal structure and zonal winds appear in Figure 10. Figure 14 shows the stationary components of the geopotential and temperature fields, plotted as longitude-height cross sections at 75°N. These were obtained by computing the time average over the full 30-sol interval and subtracting the zonal mean. We show the GCM results at 75°N rather than at the nearest grid point to the measurements, 67.5°N, because the former agree more closely with the observations. However, the results at the two latitudes are similar (see Plates 1 and 2).

The GCM reproduces several key features of the observations in Figure 6. The simulated temperature field includes strong, near-surface, wave-2 variations spanning $\sim 180°$ in longitude, with much weaker variations at other longitudes. There is agreement in both the amplitude of the near-surface temperature variations and their confinement to the lowest half scale height above the surface. The simulated geopotential field in Figure 14 also resembles the observations in Figure 8. Similarities include the deep vertical structure, the amplitude of the zonal variations ($\sim 150$ m), and the presence of a trough at the prime meridian. Near the surface the peak temperature lies about one quarter cycle westward of the peak in geopotential height, as was observed at low altitudes in Figures 11 and 12. Despite some significant differences between model and data, which are discussed below, these similarities suggest that the GCM has captured the basic character of the observed dynamics.

When displayed in a different manner, the GCM results reveal the fundamental nature of the disturbance and its probable source. Plate 1 shows a polar projection of the stationary components of geopotential height and horizontal wind at the 500-Pa pressure level, superimposed on surface topography. The geopotential field contains a distinctive pattern of peaks and troughs emanating from Alba Patera (40°N, 250°E), with alternating minima and maxima near (1) 50°N, 280°E, (2) 55°N, 315°E, (3) 73°N, 15°E, and (4) 70°N, 120°E. Item 3 is the trough that appears near the prime meridian in Figure 14. This stationary pattern appears to be a train of planetary waves excited by Alba Patera, with energy propagating eastward (counterclockwise) and poleward
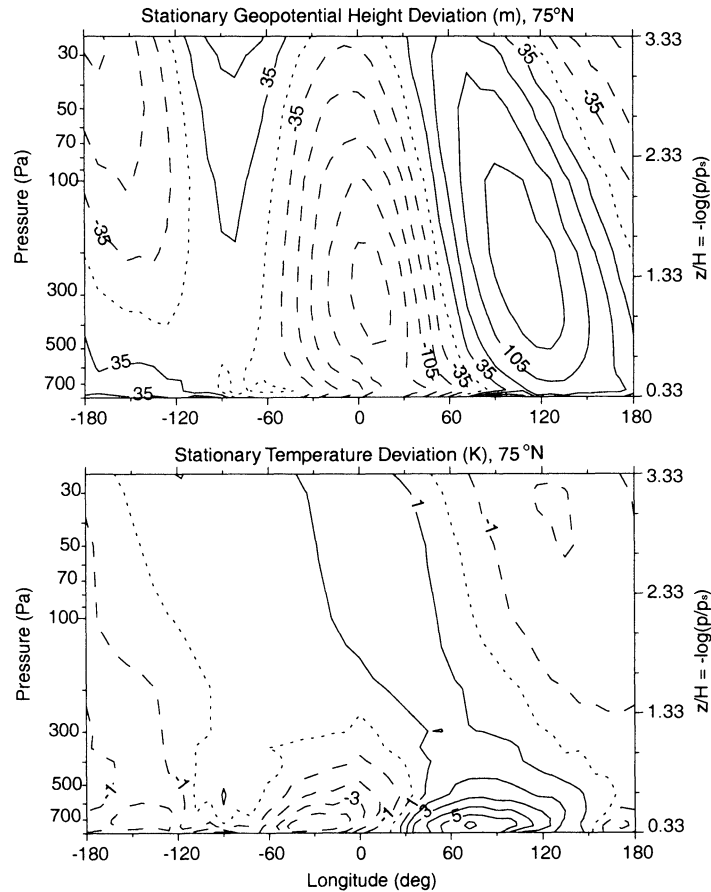
**Figure 14.** Stationary components of (top) geopotential height and (bottom) temperature at 75°N, as simulated by the NASA Ames GCM. These fields represent the time average over a 30-sol simulation; the zonal average has been subtracted. The contour intervals are 35 m and 1 K. Solid and dashed contours denote positive and negative values, respectively.

to a maximum latitude of ~75°N. This feature is remarkably similar to planetary wave trains appearing in terrestrial simulations [cf. *Hoskins and Karoly*, 1981, Figure 8d].

Plate 2 shows a polar projection of the GCM temperature and horizontal wind fields at the 700-Pa pressure level. An alternating pattern of positive and negative temperature perturbations extends eastward and northward of Alba Patera with an amplitude of ~5 K. The zonal variations of temperature (Plate 2) and geopotential (Plate 1) are in quadrature and are clearly part of the same planetary wave train. The temperature and meridional wind fields are strongly correlated, producing poleward advection of warm air and equatorward advection of cool air at the 700-Pa pressure level, as was observed (Figure 13). At 75°N the maximum and minimum GCM temperatures occur at 75°E and 330°E, respectively, corresponding to the strong near-surface temperature variations in Figure 14. The temperature variations associated with this planetary wave train are strongest over a limited range of longitudes near the surface, consistent with the observations (Figure 6).

There are several notable differences between the simulated and measured temperature fields in the lowest half scale height. Both include a temperature perturba-

tion of +6 K near 60°E, but the predominant temperature minimum appears at a different location in the simulation (~330°E) than in the measurements (~135°E). The observed and simulated patterns of near-surface temperature variations are also offset in latitude by ~8°. These differences could be due in part to errors in modeling the basic zonal wind field, which has a strong influence on the propagation of planetary waves [e.g., *Hoskins and Karoly*, 1981; *Hollingsworth and Barnes*, 1996; *Barnes et al.*, 1996]. As the offset in latitude roughly equals the grid-point spacing used in this simulation, these differences might also be a consequence of the limited spatial resolution of the GCM.

## 7. Thermal Tides

### 7.1. General Discussion

On Mars the classical Sun-synchronous thermal tides are strongly modulated by zonal variations of surface elevation, thermal inertia, and albedo, producing numerous non-Sun-synchronous modes [e.g., *Wilson and Hamilton*, 1996]. The zonal structure of each mode can be expressed as

$$Z' \propto \cos\left[s'(\lambda + 2\pi t) + s''\lambda - \epsilon_{s',s''}\right] , \qquad (12)$$

where $s'$ defines the period (1 for diurnal, 2 for semidiurnal...), $s''$ represents the effect of modulation (0, $\pm1$, $\pm2$...), $\epsilon_{s',s''}$ is the phase, and $t$ is "universal time" measured in sols (i.e., the solar time for an observer on the prime meridian). The quantity $\lambda + 2\pi t$ is an angular measure of local time on Mars. For the Sun-following diurnal tide, $s' = 1$ and $s'' = 0$. With few exceptions, these modes propagate rapidly eastward or westward relative to the surface.

The measurements in Figures 6 and 8 were acquired at nearly fixed local time. Specifically, $\lambda + 2\pi t$ drifted by only $\sim\pi/90$ per sol and therefore did not change appreciably within the 7-sol span of these experiments. When sampled in this way, the tidal modes produce a stationary pattern with zonal wave number $s = |s''|$ [cf. *Forbes and Hagan*, 2000; *Wilson*, 2000]. Hence tides could be responsible for some of the structure in Figures 6, 8, and 9.

In contrast, tides are strongly suppressed in Figure 14 and Plates 1 and 2 owing to temporal averaging. With this in mind, we examined the measurements and simulation for any differences that might be indicative of tides. The geopotential field appears to be more useful for this purpose, and the most notable discrepancy is the failure of the simulation to account for the rapid increase of wave-2 geopotential with height at pressures <200 Pa (see Figure 9). We show in section 7.2 that thermal tides are probably responsible for this feature.

## 7.2. GCM Simulation

We used the GCM of the NOAA Geophysical Fluid Dynamics Laboratory (GFDL) [*Wilson and Hamilton*, 1996] to investigate this aspect of the measured geopotential field. The results shown here are based on a version of the model with 40 vertical layers extending from the surface to 0.006 Pa and a horizontal resolution of 5° in latitude by 6° in longitude. The model topography conforms to measurements by the MGS laser altimeter [*Smith et al.*, 1999]. We tabulated results from the GFDL simulation over 10-sol intervals centered on selected values of $L_s$.

The GFDL simulation involves self-consistent advection of radiatively active aerosol [*Wilson and Hamilton*, 1996]. The dust source is specified through a model of dust devil activity, and the size distribution includes particles with radii of 0.2, 0.5, 1.0, 1.6, 2.5, and 4.0 $\mu$m. In the simulation described here, atmospheric transport is dominated by the Hadley circulation, which concentrates dust at tropical latitudes [cf. *Wilson*, 1997]. The dust opacity at low latitudes, $\sim0.3$, is close to the value adopted for the Ames GCM simulation (see section 5).

A rich spectrum of tides appears in the simulation [cf. *Wilson and Hamilton*, 1996]. The predominant non-Sun-synchronous component is an eastward propagating, diurnal, wave-1 Kelvin mode, excited by wave-2 modulation of the Sun-synchronous diurnal tide. In

the notation of (12) this corresponds to $s' = 1$ and $s'' = -2$. As explained previously, it will appear as stationary wave-2 structure in measurements at fixed local time. This Kelvin wave is near resonance in the Martian atmosphere, which accounts for its prominence [*Wilson and Hamilton*, 1996; see also *Zurek*, 1976, 1988]. This wave has been observed by the infrared sounders on both Mariner 9 [*Conrath*, 1976] and MGS [*Wilson*, 2000; *Banfield et al.*, 2000] and is believed to be responsible for the large zonal variations of density encountered by MGS during aerobraking [*Forbes and Hagan*, 2000]. Although Kelvin waves are most readily observed near the equator, this mode has a very large meridional scale and an appreciable amplitude at 66°N [cf. *Wilson*, 2000].

Figure 15 shows the simulated structure of the diurnal, wave-1 Kelvin mode (top panel) at essentially the same local time (0400), latitude (67.5°N), and season ($L_s = 75°$) as the occultation measurements. Its amplitude increases from $\sim25$ m near the surface to more than 300 m at the 1-Pa pressure level, and the vertical wavelength is very large, as expected for a nearly resonant mode. This increase of amplitude with increasing height is generally consistent with the observed behavior of wave-2 geopotential at pressures <200 Pa in Figure 9. At the 25-Pa pressure level the simulated amplitude of the Kelvin mode, $\sim60$ m, compares favorably with the measured wave-2 amplitude, $\sim100$ m.

Stationary planetary waves also appear in the GFDL simulation, and their structure is considerably different than the Kelvin mode. The stationary wave-2 component, which appears in Figure 15 (bottom panel), has an amplitude of $\sim60$ m between the surface and the 3-Pa pressure level. Its zonal variations are nearly 180° out of phase with the Kelvin mode at this local time.

The total wave-2 geopotential in the GFDL simulation is the sum of the tidal and stationary components that appear in Figure 15. These are combined and compared with the measured wave-2 component of geopotential in Figure 16. The simulated field is dominated by the diurnal, wave-1 Kelvin mode at high altitudes and by the stationary planetary wave at low altitudes, with a transition at a pressure of $\sim20$ Pa. The character of this interference pattern reflects the relative amplitude and phase of the two components, as shown in Figure 15.

A different pressure range is used for each panel of Figure 16, which serves to emphasize the similarities between the measured and simulated fields. In particular, the measured wave-2 geopotential appears to contain the same type of interference pattern as the simulation. This implies that the measured wave-2 structure includes not only a planetary-wave component at low altitudes, as discussed previously, but also a tidal component at high altitudes, with strong interference between the two at pressures near 200 Pa (see Figure 9). In support of this conclusion we note the favorable agreement between the simulated and measured phase of both components. Hence the diurnal, wave-1 Kelvin
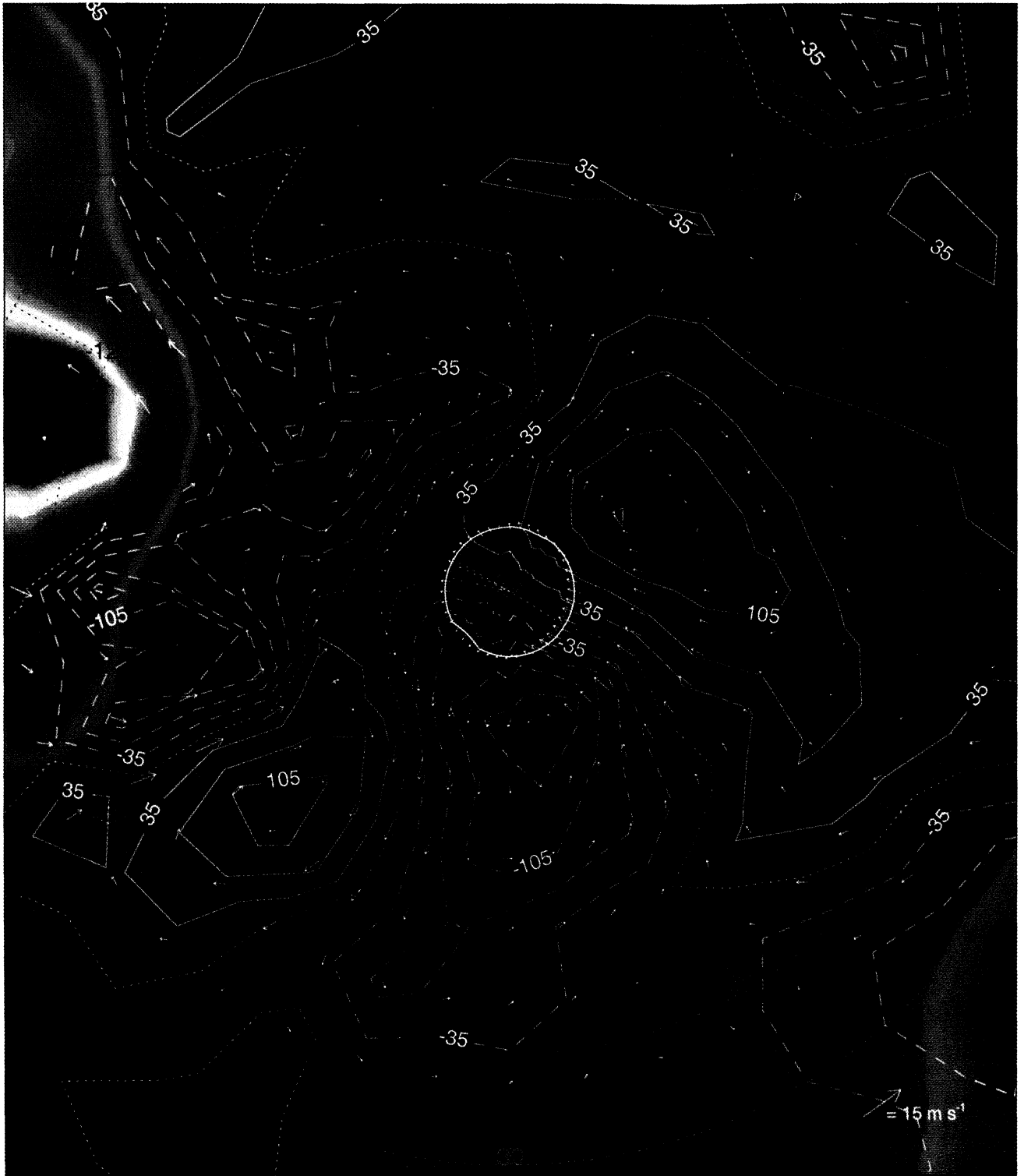
**Plate 1.** Stationary "eddy" components of geopotential height (contours) and horizontal wind (vectors) at the 500-Pa pressure level, as simulated by the NASA Ames GCM. The zonal average has been subtracted from both fields. The contour interval is 35 m, with positive and negative values depicted by solid and dashed lines, respectively. The scale for the wind vectors appears at the bottom right. The color-coded background shows the surface topography [*Smith et al.*, 1999] smoothed to the resolution of the GCM. The bright red, high-elevation feature at 40°N, 250°E is Alba Patera. The boundary of the retreating $CO_2$ polar cap is shown by a thick white line poleward of 80°N.
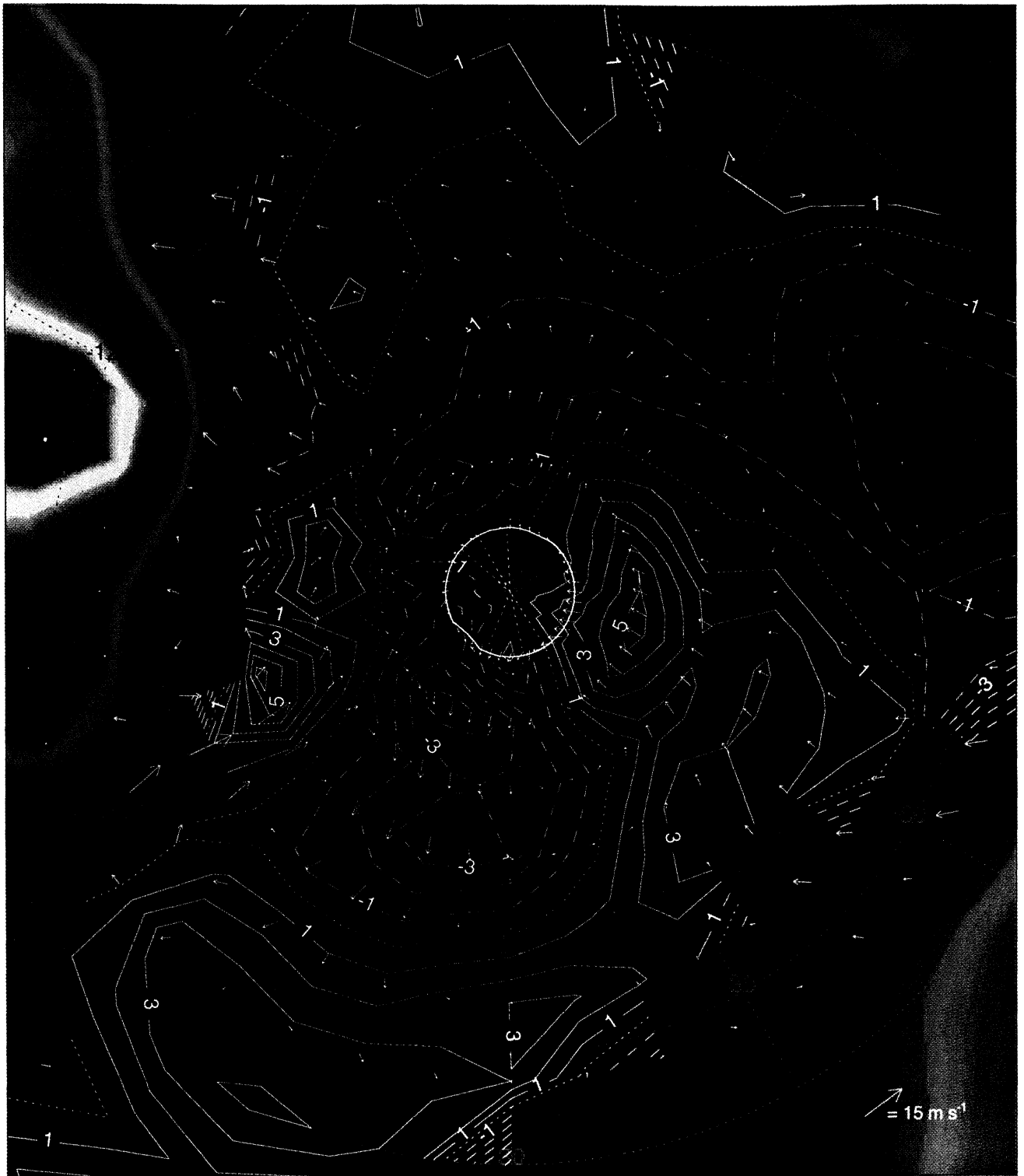
**Plate 2.** Stationary "eddy" components of temperature (contours) and horizontal wind (vectors) at the 700-Pa pressure level, as simulated by the NASA Ames GCM. The zonal average has been subtracted from both fields. Temperature contours are shown at 1-K intervals, with positive and negative values depicted by solid and dashed lines, respectively. See Plate 1 for further discussion.
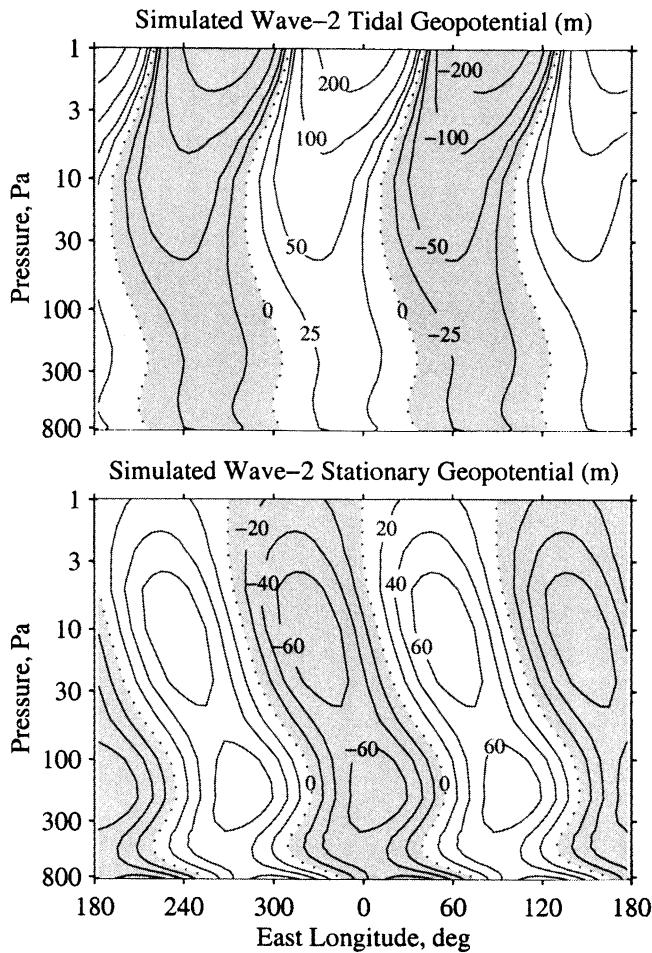
## Simulated Wave–2 Tidal Geopotential (m)



## Simulated Wave–2 Stationary Geopotential (m)



**Figure 15.** Wave-2 components of geopotential field as simulated by the GFDL GCM. Results are shown as they would appear in measurements at a fixed local time of 0400 at 67.5°N for $L_s = 75°$. The total field has been separated into (top) tidal and (bottom) stationary components. The tidal component is dominated by the resonantly enhanced, diurnal, wave-1 Kelvin mode, while the stationary component is a planetary wave. The contour interval is (top) nonuniform and (bottom) 20 m. Shading denotes negative values.

mode appears to be responsible for the observed behavior of wave-2 geopotential at pressures <200 Pa.

The comparison in Figure 16 also reveals significant differences. The signature of the Kelvin mode extends to a much greater pressure in the measurements (~200 Pa) than in the simulation (~20 Pa). This discrepancy probably reflects the difficulty inherent in simulations involving destructive interference. Additional insight can be gained by examining the GFDL simulation at different values of $L_s$. Between $L_s = 66°$ and 88° the simulation indicates that the amplitude of the planetary waves decays with season while the amplitude of the Kelvin mode simultaneously increases. The resulting interference pattern evolves with time in response to contributions from two diverse, seasonally varying components.

## 8. Discussion

In this paper a small set of high-quality occultation measurements has yielded new insight into the behavior of both stationary planetary waves and thermal tides on Mars. The value of these data is greatly enhanced through the use of two GCMs. The experience gained from this collaboration provides a foundation for future work involving much larger quantities of MGS occultation data.

There is very little baroclinic eddy activity at the latitude and season of these measurements, as reflected by the absence of significant day-to-day variation in thermal structure (see Figures 4 and 5). This conclusion is supported by both of our GCM simulations. Hub-
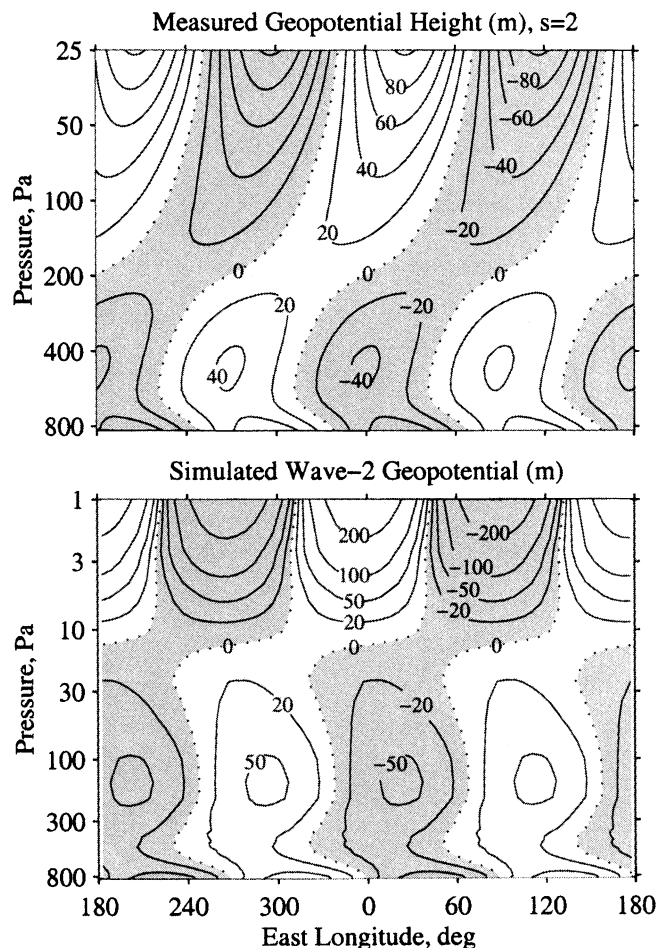
## Measured Geopotential Height (m), s=2



## Simulated Wave–2 Geopotential (m)



**Figure 16.** (top) Wave-2 component of measured geopotential field, which appeared previously in Figure 12. The contour interval is 20 m. Shading denotes negative values. (bottom) Total wave-2 geopotential field as simulated by the GFDL GCM. The total field is the sum of the tidal and stationary components displayed in Figure 15. Results are shown as they would appear in measurements at a fixed local time of 0400 at 67.5°N for $L_s = 75°$. The contour interval is nonuniform. Note that a different pressure range is used for each panel.

ble Space Telescope images and previous GCM simulations suggest that strong transient eddies appear at this latitude in early northern spring [*James et al.*, 1999], with vigorous meridional winds near the boundary of the retreating seasonal polar cap [*Hollingsworth et al.*, 1997]. This activity appears to have vanished at 66°N by $L_s = 75°$.

The behavior of planetary waves in late northern spring, as illustrated in Figure 14 and Plates 1 and 2, is considerably different than what appears in winter-solstice simulations [e.g., *Hollingsworth and Barnes*, 1996; *Barnes et al.*, 1996]. In winter the mean zonal wind field is far more conducive to vertical propagation, resulting in planetary waves that extend to much higher altitudes and have much larger amplitudes than in late spring. In addition, planetary waves in winter simulations tend to be fully developed in longitude, contrasting with the wave-train character of the disturbance in Plates 1 and 2. These differences reflect the seasonal evolution of planetary waves on Mars.

This characterization of forced atmospheric waves may contribute to an improved understanding of the seasonal water cycle. At 66°N in late spring the water vapor content of the atmosphere is increasing rapidly as the seasonal polar cap retreats and the residual ice cap becomes exposed [e.g., *Jakosky and Haberle*, 1992]. According to measurements by the Viking Orbiters, the column content at 66°N increases from the equivalent of ~1 $\mu$m of liquid water at $L_s = 0°$ to ~30 $\mu$m at $L_s = 75°$ [*Jakosky and Farmer*, 1982]. Meridional advection by "eddies" is suspected to be an important component of the water cycle [*Leovy*, 1973; *Barnes*, 1990; *Jakosky and Haberle*, 1992; *Houben et al.*, 1997; *Richardson*, 1999], particularly near northern summer solstice. The results reported here provide new constraints for future GCM simulations.

# References

Albee, A. L., F. D. Palluconi, and R. E. Arvidson, Mars Global Surveyor Mission: Overview and status, *Science, 279*, 1671-1672, 1998.

Andrews, D. G., J. R. Holton, and C. B. Leovy, *Middle Atmosphere Dynamics*, 489 pp., Academic, San Diego, Calif., 1987.

Banfield, D., A. D. Toigo, A. P. Ingersoll, and D. A. Paige, Martian weather correlation length scales, *Icarus, 119*, 130-143, 1996.

Banfield, D., B. Conrath, J. C. Pearl, M. D. Smith, and P. Christensen, Thermal tides and stationary waves on Mars as revealed by Mars Global Surveyor Thermal Emission Spectrometer, *J. Geophys. Res., 105*, 9521-9537, 2000.

Barnes, J. R., Transport of dust to high northern latitudes in a Martian polar warming, *J. Geophys. Res., 95*, 1381-1400, 1990.

Barnes, J. R., R. M. Haberle, J. B. Pollack, H. Lee, and J. Schaeffer, Mars atmospheric dynamics as simulated by the NASA Ames general circulation model, 3, Winter quasi-stationary eddies, *J. Geophys. Res., 101*, 12,753-12,776, 1996.

Conrath, B. J., Influence of planetary-scale topography on the diurnal thermal tide during the 1971 Martian dust storm, *J. Atmos. Sci., 33*, 2430-2439, 1976.

Conrath, B. J., Planetary-scale wave structure in the Martian atmosphere, *Icarus, 48*, 246-255, 1981.

Davies, M. E., et al., Report of the IAU/IAG/COSPAR working group on cartographic coordinates and rotational elements of the planets and satellites: 1991, *Celest. Mech. Dyn. Astron., 53*, 377-397, 1992.

Fjeldbo, G., and V. R. Eshleman, The atmosphere of Mars analyzed by integral inversion of the Mariner IV occultation data, *Planet. Space Sci., 16*, 1035-1059, 1968.

Fjeldbo, G., A. J. Kliore, and V. R. Eshleman, The neutral atmosphere of Venus as studied with the Mariner 5 radio occultation experiments, *Astron. J., 76*, 123-140, 1971.

Forbes, J. M., and M. E. Hagan, Diurnal Kelvin wave in the atmosphere of Mars: Towards an understanding of 'stationary' density structures observed by the MGS accelerometer, *Geophys. Res. Lett., 27*, 3563-3566, 2000.

Forget, F., F. Hourdin, R. Fournier, C. Hourdin, O. Talagrand, M. Collins, S. R. Lewis, P. L. Read, and J.-P. Huot, Improved general circulation models of the Martian atmosphere from the surface to above 80 km, *J. Geophys. Res., 104*, 24,155-24,175, 1999.

Haberle, R. M., J. B. Pollack, J. R. Barnes, R. W. Zurek, C. B. Leovy, J. R. Murphy, H. Lee, and J. Schaeffer, Mars atmospheric dynamics as simulated by the NASA Ames general circulation model, 1, The zonal-mean circulation, *J. Geophys. Res., 98*, 3093-3123, 1993.

Haberle, R. M., M. M. Joshi, J. R. Murphy, J. R. Barnes, J. T. Schofield, G. Wilson, M. Lopez-Valverde, J. L. Hollingsworth, A. F. C. Bridger, and J. Schaeffer, General circulation model simulations of the Mars Pathfinder atmospheric structure investigation/meteorology data, *J. Geophys. Res., 104*, 8957-8974, 1999.

Hess, S. L., R. M. Henry, C. B. Leovy, J. A. Ryan, and J. E. Tillman, Meteorological results from the surface of Mars: Viking 1 and 2, *J. Geophys. Res., 82*, 4559-4574, 1977.

Hinson, D. P., R. A. Simpson, J. D. Twicken, G. L. Tyler, and F. M. Flasar, Initial results from radio occultation measurements with Mars Global Surveyor, *J. Geophys. Res., 104*, 26,997-27,012, 1999.

Hollingsworth, J. L., and J. R. Barnes, Forced stationary planetary waves in Mars's winter atmosphere, *J. Atmos. Sci., 53*, 428-448, 1996.

Hollingsworth, J. L., R. M. Haberle, and J. Schaeffer, Seasonal variations of storm zones on Mars, *Adv. Space Res., 19(8)*, 1237-1240, 1997.

Holton, J. R., *An Introduction to Dynamic Meteorology*, 3rd ed., 511 pp., Academic, San Diego, Calif., 1992.

Hoskins, B. J., and D. J. Karoly, The steady linear response of a spherical atmosphere to thermal and orographic forcing, *J. Atmos. Sci., 38*, 1179-1196, 1981.

Houben, H., R. M. Haberle, R. E. Young, and A. P. Zent, Modeling the Martian seasonal water cycle, *J. Geophys. Res., 102*, 9069-9083, 1997.

Hourdin, F., P. Le Van, F. Forget, and O. Talagrand, Meteo-

rological variability and the annual surface pressure cycle on Mars, *J. Atmos. Sci., 50,* 3625-3640, 1993.

Jakosky, B. M., and C. B. Farmer, The seasonal and global behavior of water vapor in the Mars atmosphere: Complete global results of the Viking atmospheric water detector experiment, *J. Geophys. Res., 87,* 2999-3019, 1982.

Jakosky, B. M., and R. M. Haberle, The seasonal behavior of water on Mars, in *Mars,* edited by H. H. Kieffer et al., pp. 969-1016, Univ. of Ariz. Press, Tucson, 1992.

James, P. B., J. L. Hollingsworth, M. J. Wolff, and S. W. Lee, North polar dust storms in early spring on Mars, *Icarus, 138,* 64-73, 1999.

Karayel, E. T., and D. P. Hinson, Sub-Fresnel-scale vertical resolution in atmospheric profiles from radio occultation, *Radio Sci., 32,* 411-423, 1997.

Leovy, C. B., Exchange of water vapor between the atmosphere and surface of Mars, *Icarus, 18,* 120-125, 1973.

Leovy, C. B., Martian meteorology, *Annu. Rev. Astron. Astrophys., 17,* 387-413, 1979.

Leovy, C. B., Observations of Martian tides over two annual cycles, *J. Atmos. Sci., 38,* 30-39, 1981.

Leovy, C. B., and R. W. Zurek, Thermal tides and Martian dust storms: Direct evidence for coupling, *J. Geophys. Res., 84,* 2956-2968, 1979.

Leovy, C. B., J. E. Tillman, W. R. Guest, and J. Barnes, Interannual variability of Martian weather, in *Recent Advances in Planetary Meteorology,* edited by G. E. Hunt, pp. 69-84, Cambridge Univ. Press, New York, 1985.

Lomb, N. R., Least-squares frequency analysis of unequally spaced data, *Astrophys. Space Sci., 39,* 447-462, 1976.

Martin, T. Z., and H. Kieffer, Thermal infrared properties of the Martian atmosphere, 2, The 15 $\mu$m band measurements, *J. Geophys. Res., 84,* 2843-2852, 1979.

Nayvelt, L., P. J. Gierasch, and K. H. Cook, Modeling and observations of Martian stationary waves, *J. Atmos. Sci., 54,* 986-1013, 1997.

Pirraglia, J. A., and B. J. Conrath, Martian tidal pressure and wind fields obtained from the Mariner 9 infrared spectroscopy experiment, *J. Atmos. Sci., 31,* 318-329, 1974.

Pollack, J. B., C. B. Leovy, P. W. Greiman, and Y. Mintz, A Martian general circulation experiment with large topography, *J. Atmos. Sci., 38,* 3-29, 1981.

Pollack, J. B., R. M. Haberle, J. Schaeffer, and H. Lee, Simulations of the general circulation of the Martian atmosphere, 1, Polar processes, *J. Geophys. Res., 95,* 1447-1473, 1990.

Pollack, J. B., R. M. Haberle, J. R. Murphy, J. Schaeffer, and H. Lee, Simulations of the general circulation of the Martian atmosphere, 2, Seasonal pressure variations, *J. Geophys. Res., 98,* 3149-3181, 1993.

Press, W. H., and S. A. Teukolsky, Search algorithm for weak periodic signals in unevenly spaced data, *Computers in Physics, 2,* 77-82, 1988.

Richardson, M. I., Comparison of microwave and infrared measurements of Martian atmospheric temperatures: Implications for short-term climate variability, *J. Geophys. Res., 103,* 5911-5918, 1998.

Richardson, M. I., A general circulation model study of the Mars water cycle, Ph.D. thesis, 220 pp., Univ. of Calif., Los Angeles, March 1999.

Santee, M., and D. Crisp, Thermal structure and dust loading of the Martian atmosphere during late southern summer: Mariner 9 revisited, *J. Geophys. Res., 98,* 3261-3279, 1993.

Santee, M. L., and D. Crisp, Diagnostic calculations of the circulation in the Martian atmosphere, *J. Geophys. Res., 100,* 5465-5484, 1995.

Smith, D. E., F. J. Lerch, R. S. Nerem, M. T. Zuber, G. B. Patel, S. K. Fricke, and F. G. Lemoine, An improved gravity model for Mars: Goddard Mars model 1, *J. Geophys. Res., 98,* 20,871-20,889, 1993.

Smith, D. E., et al., The global topography of Mars and implications for surface evolution, *Science, 284,* 1495-1503, 1999.

Tyler, G. L., G. Balmino, D. P. Hinson, W. L. Sjogren, D. E. Smith, R. Woo, S. W. Asmar, M. J. Connally, C. L. Hamilton, and R. A. Simpson, Radio science investigations with Mars Observer, *J. Geophys. Res., 97,* 7759-7779, 1992.

Webster, P. J., The low-latitude circulation of Mars, *Icarus, 30,* 626-649, 1977.

Wilson, R. J., A general circulation model simulation of the Martian polar warming, *Geophys. Res. Lett., 24,* 123-126, 1997.

Wilson, R. J., Evidence for diurnal period Kelvin waves in the Martian atmosphere from Mars Global Surveyor TES data, *Geophys. Res. Lett., 27,* 3889-3892, 2000.

Wilson, R. J., and K. Hamilton, Comprehensive model simulation of thermal tides in the Martian atmosphere, *J. Atmos. Sci., 53,* 1290-1326, 1996.

Wilson, R. J., and M. I. Richardson, The Martian atmosphere during the Viking mission, 1, Infrared measurements of atmospheric temperatures revisited, *Icarus, 145,* 555-579, 2000.

Wu, D. L., P. B. Hays, and W. R. Skinner, A least squares method for spectral analysis of space-time series, *J. Atmos. Sci., 52,* 3501-3511, 1995.

Zurek, R. W., Diurnal tide in the Martian atmosphere, *J. Atmos. Sci., 33,* 321-337, 1976.

Zurek, R. W., Free and forced modes in the Martian atmosphere, *J. Geophys. Res., 93,* 9452-9462, 1988.

Zurek, R. W., and C. B. Leovy, Thermal tides in the dusty Martian atmosphere: A verification of theory, *Science, 213,* 437-439, 1981.

D. P. Hinson and G. L. Tyler, Department of Electrical Engineering, Stanford University, 350 Serra Mall, Stanford, CA 94305-9515. (hinson@nimbus.stanford.edu)

J. L. Hollingsworth, NASA Ames Research Center, MS 245-3, Moffett Field, CA 94035-1000. (jeffh@humbabe.arc.nasa.gov)

R. J. Wilson, Geophysical Fluid Dynamics Laboratory (NOAA), P.O. Box 308, Princeton University Forrestal Campus, Princeton, NJ 08542. (rjw@gfdl.gov)